

# Design of high-performance sintered-wick heat pipes

D. A. PRUZAN, L. K. KLINGENSMITH, K. E. TORRANCE and  
C. T. AVEDISIAN

Sibley School of Mechanical and Aerospace Engineering, Cornell University, Ithaca,  
NY 14853, U.S.A.

(Received 29 November 1989 and in final form 10 July 1990)

**Abstract**—An analytical model for predicting peak (dryout) steady-state heat transfer limits in heat pipes utilizing sintered-wick structures is presented. Boiling is accounted for and one-dimensional liquid and vapor flows are assumed. Experimental measurements of peak heat flux values for two cylindrical sintered-copper wicks are made and compared with analytical predictions. Theoretical and experimental dryout heat flux values agree to within 10%. Using the analytical model, flat plate and cylindrical wick heat pipe performance is evaluated as a function of design parameters. Parameters for high-performance flat plate and cylindrical wicks are identified. Peak heat fluxes up to 50 and 100 W cm<sup>-2</sup>, respectively, are predicted for 10 cm long high-performance wicks using water as the coolant.

## INTRODUCTION

HEAT PIPES have been used for the thermal management of cold weather gloves for humans, blast furnaces, space systems, and VHSIC (very high speed integrated circuit) computer chips [1-4]. Heat pipes often involve active boiling in the liquid-return wick, such that dryout of the wick can be performance limiting. The present paper reports an analytical and experimental study of dryout in heat pipe wicks, and a parametric design study to achieve high-performance wicks. The study is motivated by the needs of the electronics industry.

Advances in semiconductor design have led to projected heat fluxes of 50 W cm<sup>-2</sup> at the chip level with temperatures limited to 100°C [5]. Forced-air convective cooling may not be capable of meeting these demands. One alternative is a liquid-cooled, single-phase, thermal conduction module, capable of transferring 20 W cm<sup>-2</sup> at the chip level [6, 7]. An alternative approach for liquid cooling is the heat pipe. A flat plate heat pipe design suitable for chip cooling is sketched in Fig. 1. High chip heat fluxes are used to boil saturated liquid coolant from a porous wick structure. The resulting vapor travels out of the wick and condenses on a low-heat-flux condensing surface. The condensate re-enters the wick and is returned to the chip site by capillary action of the wick. Flat plate heat pipes have recently been developed for avionic applications [8].

Most currently-available heat pipes which are capable of meeting the heat transfer requirements projected by the electronics industry tend to operate in a temperature range beyond that acceptable for electronic components. We have studied the possibility of creating high-heat-flux, low-temperature ( $\approx 100^\circ\text{C}$ ) heat pipes through the use of optimized wick structure

design. A model for predicting peak steady-state heat flux limits (dryout heat flux, DHF) as a function of wick structure parameters, capillary pumping requirements, and the liquid coolant is presented in this paper. The model is a combination of one-dimensional, single- and two-phase flow models from refs. [9-11] and wick structure models from ref. [12]. Both flat plate and cylindrical sintered-wick heat pipes can be simulated.

Peak heat transfer rates were also experimentally collected for two cylindrical sintered-copper wicks for comparison with results from the model. Predicted DHF values are shown to agree with experimentally measured values to within 10%. Results from the analytical parameter study were used to design flat plate and cylindrical wick structures theoretically capable of dissipating heat fluxes up to 50 and 100 W cm<sup>-2</sup>, respectively, with water as the coolant.

## EXPERIMENT

### Apparatus

Dryout heat flux values were measured for two everted cylindrical sintered-copper wicks using the apparatus functionally depicted in Fig. 2. Coolant enters the porous wick from a liquid pool surrounding the base of the wick/support tube assembly. Capillary action draws the liquid coolant upwards against gravity to the heated section where it is boiled by a uniform flux heater of length  $L_h$  and diameter  $D$ , 6.4 and 1.28 cm, respectively. The resulting vapor travels horizontally out of the porous structure and is condensed externally on the walls of an airtight cylindrical glass chamber enclosing the wick. The wick structure is fixed in a vertical orientation with capillary pumping requirements varied by changing the capillary rise



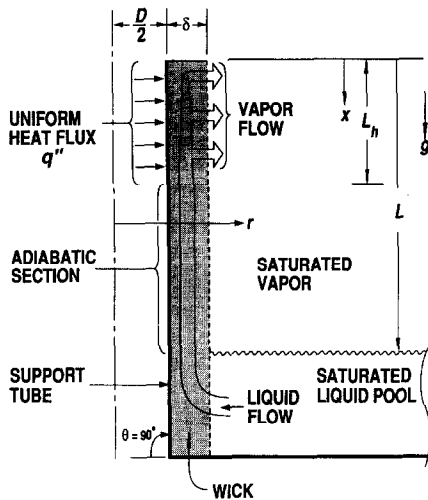


FIG. 2. Everted cylindrical heat pipe geometry for experimental and analytical work, utilizing a fixed tilt angle ( $\theta = 90^\circ$ ) and variable capillary rise height,  $L$ .

the central tube. The external sleeves were removed, leaving finished wick/tube assemblies.

#### Wick properties

Internal characteristics of the porous wick structures, such as capillary radius of curvature of the pores,  $r_c$ , porosity,  $\varepsilon$ , and bulk permeability,  $k$ , must be known in order to specify the flow characteristics of the wicks. Capillary radius of curvature is primarily a function of the average particle size. Porosity is a function of the particle size distribution, with a tighter distribution tending towards higher porosities [15]. The bulk permeability can be related to  $\varepsilon$  and  $r_c$  with the Kozeny-Carman relation [15]

$$k = \frac{4(r_c)^2}{180} \frac{\varepsilon^3}{(1-\varepsilon)^2} \quad (1)$$

The procedures for obtaining  $r_c$ ,  $\varepsilon$ ,  $k$  and the dryout heat flux are described in the following sections. The physical properties of the two sintered wicks are summarized in Table 1. Further details are available in refs. [13, 14].

#### Measurement of $r_c$

The capillary radius of curvature of each wick was obtained experimentally. The maximum static hold-up height,  $L_{hu}$ , was measured with the apparatus

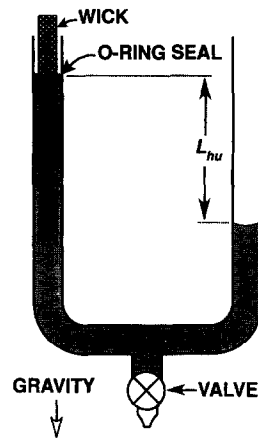


FIG. 3. Apparatus for determining the effective capillary radius of curvature,  $r_c$ .

shown in Fig. 3. Capillary pressure generated by the porous structure was used to maintain a column of fluid in the left branch of the U-tube as fluid was drained from the system in steps. Enough time was allowed between steps for the system to reach equilibrium. A run was concluded when the fluid column in the left branch of the U-tube collapsed. The value of  $L_{hu}$  thus measured was used to determine the maximum capillary pressure,  $P_c$ , and a tentative estimate of the radius of curvature from equations (2) and fluid property data

$$P_c = \rho_l g L_{hu} \quad (2a)$$

$$r_c = \frac{2\sigma}{P_c} \quad (2b)$$

The value for radius of curvature obtained in this manner incorporates the variations of capillary radius within the wick structure and the surface tension interactions between the fluid and sintered material. This experimentally-inferred value will be referred to as the *effective* capillary radius of curvature.

#### Measurement of DHF and $k$

The procedure to obtain the bulk permeability is somewhat more involved, and is based on experimental measurements of DHF. In the experiments, the  $q''-\Delta T$  behavior was plotted, where  $q''$  is the heat flux at the surface of the heater and  $\Delta T$  the difference between the average heater surface temperature and the fluid saturation temperature. In general,  $q''$  increased approximately linearly with  $\Delta T$  up to a

Table 1. Wick structure parameters for the two sintered-copper wicks

	Wick thickness, $\delta$ (cm)	Inner diameter, $D$ (cm)	Permeability $k$ ( $\text{cm}^2$ )	Effective capillary radius $r_c$ (cm)	Porosity, $\varepsilon$ (%)
Wick #1	0.076	1.28	$1.050 \times 10^{-7}$	$2.05 \times 10^{-3}$	58
Wick #2	0.318	1.28	$1.996 \times 10^{-7}$	$2.58 \times 10^{-3}$	60

break point. At the break point, larger increases in  $\Delta T$  were observed with small increases in  $q''$ . The breakpoint was identified as the dryout heat flux for the wick. DHF values were measured as a function of capillary rise height  $L_h$  [13]. Related results for a screen mesh wick are reported in ref. [12]. Both studies used water, ethanol, and their mixtures as working fluids.

A simple theory is available [9] which relates the bulk permeability to DHF at large values of the capillary rise height. In this limit, it is assumed that the pressure drop encountered by the fluid is due to gravity and viscous flow through the wick. The pressure drop due to two-phase flow in the heated section is neglected. Under these conditions, the dryout heat flux can be equated to the product of the maximum liquid mass flow rate through the wick and the latent heat of vaporization of the coolant. The maximum liquid flow rate is found, in turn, by equating the peak capillary pressure in the wick to the pressure drop associated with single-phase liquid flow through the wick. Combining these relations, there results

$$\text{DHF} = k\psi \left[ \frac{L_{hu} - \frac{L_h}{2}}{L - \frac{L_h}{2}} - 1 \right]$$

$$\text{where } \psi = \left[ \left( \frac{A_w}{A_h} \right) \left( \frac{(\rho_l)^2 g h_{fg}}{\mu_l} \right) \right]. \quad (3)$$

This expression relates DHF to  $k$ ,  $L_{hu}$ , the heater length,  $L_h$ , and the capillary rise height,  $L$ .

When fluid and wick properties are constant, equation (3) predicts a linear relationship between DHF and  $1/(L - L_h/2)$ . This linear behavior may be expected to describe experimental DHF data only when the capillary rise height is large (i.e.  $L \gg L_h$ ) and the two-phase pressure drop is small. Under such conditions, a linear best-fit line drawn through the measured large- $L$  DHF data and the previously measured  $L_{hu}$  value (plotted on the abscissa) can be used with equation (3) to determine an effective  $L_{hu}$  and bulk permeability. The effective  $L_{hu}$  is then used with equation (2) to find the effective capillary pressure.

Dryout heat flux data are plotted against  $1/(L - L_h/2)$  in Fig. 4 for sintered wicks #1 and #2. Data could not be obtained at large enough  $L$  values to draw accurate straight 'single-phase' lines. Cubic polynomial curves were best fit to the measured DHF and  $L_{hu}$  data and 'single-phase' lines were drawn tangent to the cubic fit curves at DHF = 0. The 'single-phase' lines were used with equations (2) and (3) to determine the effective capillary radius of curvature and the bulk permeability values listed in Table 1. Note that for sintered wick #1, Fig. 4(a), the resulting straight line provides a good fit to the two lowest DHF points suggesting that these points are in the linear region described by equation (3).

#### Wick porosity, $\epsilon$

Wick porosity was not measured directly but was inferred from the measurements of  $k$  and  $r_c$  using the Kozeny-Carmen relation, equation (1). The resulting values of  $\epsilon$  are listed in Table 1. Note that the porosity values are in qualitative agreement with the scanning electron microscope photographs shown in Fig. 5. Furthermore, the effective capillary radius of curvature values,  $r_c$ , listed in Table 1 are also in qualitative accord with the photographs. The photographs in Fig. 5 were taken after the completion of the boiling experiments.

## THEORY

### Formulation

Single- and two-phase analytical models have been proposed for predicting dryout heat flux values in screen-wick and sintered-wick heat pipes [9–12]. The present two-phase model for sintered-wick heat pipes assumes that most system variables are functions of the  $x$ -coordinate only [11] (see Fig. 2). For cylindrical geometries an exception is the cross flowing vapor velocity which, from continuity, must also vary with radius. Thermal equilibrium between liquid and vapor is assumed at the saturation temperature corresponding to the system operating pressure. Thermal conduction across the wick is neglected and all energy transfer within the wick is assumed to result from phase change at the heated wall [10, 11]. Further, fluid flow is governed by the Darcy momentum equations taking into account reduced permeabilities when both phases are present. Relative permeabilities for liquid and vapor are assumed to be cubic functions of the local saturation,  $S$  [16]. Capillary pressure,  $P_c$ , is assumed to be constant [11, 12], as are all fluid and wick properties. The resulting governing equations are written in a form suitable for both cylindrical and flat plate ( $D = \text{infinity}$ ) geometries. Heat pipes with fixed rise height,  $L$ , and variable tilt angle,  $\theta$ , Fig. 1, or fixed tilt angle and variable rise height, Fig. 2, can be simulated. The latter geometry is similar to that used in the experiment and is employed in the following analysis.

### Governing equations

Flow in the adiabatic section is governed by the single-phase Darcy momentum equation, given by

$$U = - \frac{k}{\mu_l} \left[ \frac{dP_l}{dx} - \rho_l g \sin \theta \right] \quad (4)$$

where  $U$  is the liquid-phase Darcy superficial velocity in the  $x$ -direction.

In the heated section, the vapor production rate is governed by the applied heat flux through the energy equation (neglecting conduction)

$$q'' = \frac{\dot{M}_v h_{fg}}{A_h} \quad (5)$$

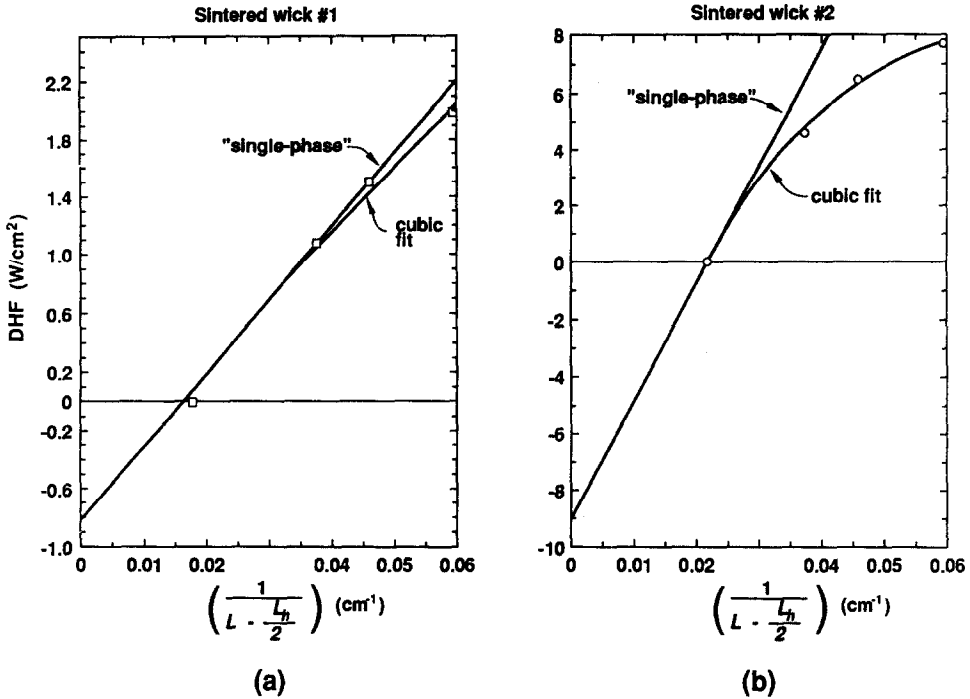


FIG. 4. Cubic fit curves of the experimental DHF data and 'single-phase' straight lines: (a) wick # 1; (b) wick # 2.

where  $\dot{M}_v$  is the mass flow rate of vapor in the  $r$ -direction. From equation (5) and the principle of vapor conservation, the superficial vapor velocity in the  $r$ -direction,  $V$ , can be found as a function of  $r$ . The liquid continuity and the two-phase Darcy momentum equations in the heated section are

$$0 = -\frac{\dot{M}_v}{A_h} + \rho_l \delta \left[ \frac{\delta}{D} + 1 \right] \frac{dU}{dx} \quad (6)$$

$$U = -\frac{kk_l}{\mu_l} \left[ \frac{dP_l}{dx} - \rho_l g \sin \theta \right] \quad (7a)$$

$$V = -\frac{kk_v}{\mu_v} \frac{dP_v}{dr} \quad (7b)$$

where the liquid and vapor pressures are denoted by  $P_l$  and  $P_v$ . With  $V$  found from equation (5) and vapor continuity, an effective vapor pressure,  $\bar{P}_v$ , can be obtained by integrating equation (7b) across the wick thickness  $\delta$

$$\bar{P}_v = P_{sat} + \frac{\dot{M}_v \mu_v}{2\pi k k_v \rho_v L_h} \ln \left( \frac{D+2\delta}{D} \right). \quad (8)$$

Additional relations are needed to complete the problem specification. The liquid and vapor relative permeabilities,  $k_l$  and  $k_v$ , are assumed to be cubic functions of the local liquid saturation,  $S$

$$k_l = S^3 \quad (9a)$$

$$k_v = (1-S)^3. \quad (9b)$$

The difference between  $P_v$  and  $P_l$  is the capillary pressure  $P_c$ , which, from equation (2), can be related to  $r_c$  and  $\sigma$  by

$$P_v - P_l = P_c = \frac{2\sigma}{r_c}. \quad (10)$$

The effective pressure given by equation (8) is used to evaluate  $P_v$ . The capillary pressure  $P_c$  is assumed to be constant throughout the wick. The capillary radius of curvature usually varies within a wick structure, but a single *effective* value is used in the present model.

The cubic relative permeability/constant capillary pressure formulation of equations (9) and (10) was used previously for simulating the peak heat flux in a screen-wick heat pipe [12]. This particular combination was selected after comparing analytical predictions from seven different relative permeability/capillary pressure models against experimental data (see refs. [12, 14] for details). Only accepted models from the porous media literature were considered. Application of the cubic permeability/constant capillary pressure formulation to the sintered-wick heat pipes of the present study appears to be justified by the agreement between experiment and theory.

*Solution method*

Five unknowns appear in equations (4)–(10); namely,  $U$ ,  $V$ ,  $P_v$ ,  $P_l$  and  $S$ . All variables in the heated

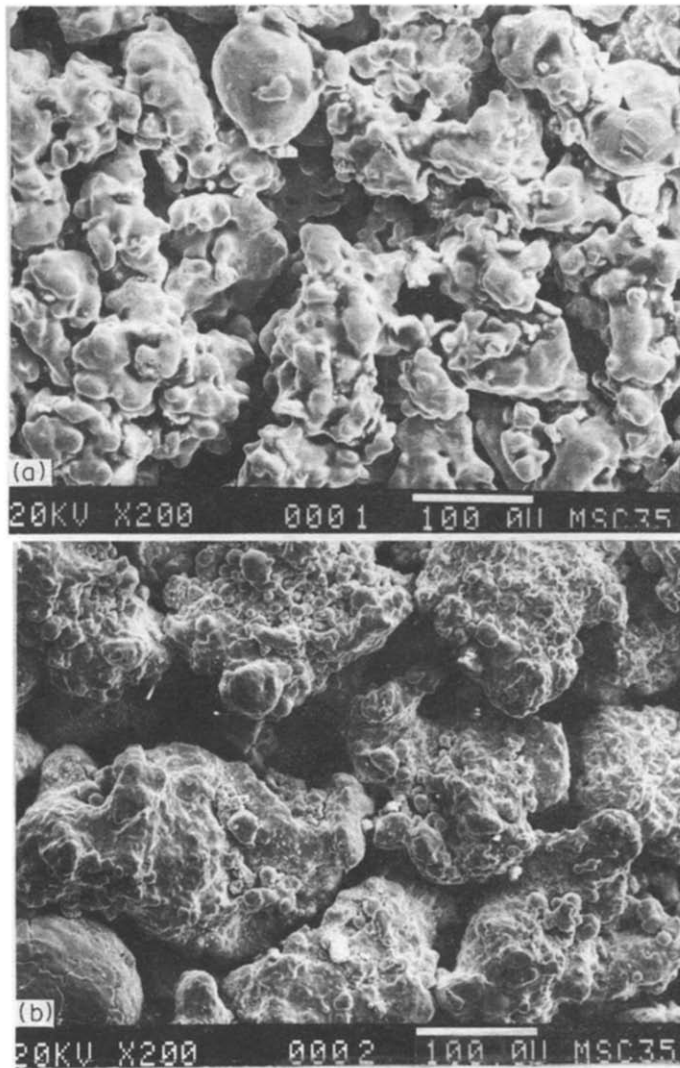


FIG. 5. Scanning electron microscope pictures at  $200\times$  magnification. The white bars at the lower right represent  $100\ \mu\text{m}$  ( $0.01\ \text{cm}$ ): (a) wick #1; (b) wick #2.

section depend on  $x$ , and  $V$  depends on  $r$  as well. The equations were solved as a function of the applied heat flux,  $q''$ , using known wick geometry, wick/fluid properties, and capillary rise height. The liquid velocity  $U$  through the adiabatic section was determined from global heat and mass balances on the heated section, since the inflow of liquid to the heated section must just balance the production of vapor in that section. Liquid pressure at the base of the heated section was found by integrating equation (4). Equations (6)–(10) are strongly nonlinear and were solved by finite difference techniques. The solution was marched upwards from the base of the heated section using liquid velocity and pressure at the base of the heated section as boundary conditions. An adjustable step size was used to ensure accurate evaluation of pressure and saturation gradients. The dryout heat flux was assumed to be reached when the local steady-state saturation at the top of the heated section reached an irreducible liquid saturation level,  $S_{\text{irr}}$ .

Actual  $S_{\text{irr}}$  values for the two experimental wicks were not available, but as shown in Table 2, DHF is relatively insensitive to  $S_{\text{irr}}$ . A value of 1% was therefore assumed.

### Results

Representative normalized velocity, pressure and saturation distributions for the liquid in the heated section at dryout conditions are shown in Fig. 6.

Table 2. Influence of  $S_{\text{irr}}$  on predicted DHF for wick #2

Capillary rise height, $L$ (cm)	DHF ( $\text{W cm}^{-2}$ ) with $S_{\text{irr}}$ set to		
	1.00%	10.0%	20.0%
6.4	18.0132	18.0124	17.9975
10.0	14.2634	14.2627	14.2510
15.0	10.4928	10.4922	10.4830
20.0	7.7626	7.7620	7.7540
25.0	5.6910	5.6903	5.6825
30.0	4.0603	4.0595	4.0520

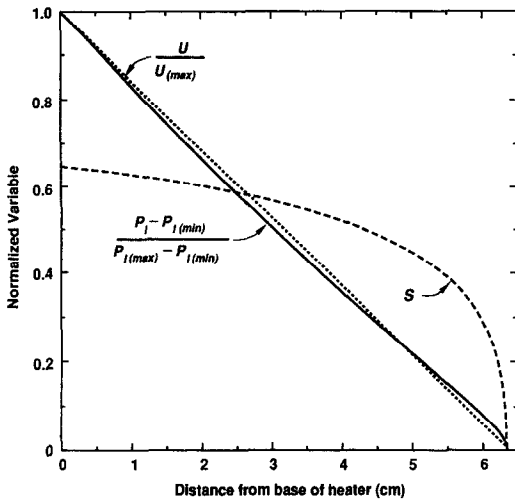


FIG. 6. Normalized liquid-phase velocity, pressure and saturation profiles in the heated section at DHF conditions for wick #2 with  $L = 10$  cm.

Results pertain to wick #2 with  $L = 10$  cm. The linear decrease in superficial liquid velocity across the heated section follows from the uniform heat flux condition and the neglect of heat conduction in the wick. The vapor velocity is also constant along the entire heated length. The step decrease in liquid saturation at the base of the heater arises in order to generate sufficient local vapor relative permeabilities commensurate with the vapor velocity and the local effective vapor pressure.

Experimentally-measured values of DHF for the two sintered wicks are shown in Fig. 7. The solid lines are best-fit lines through the experimental data. The predictions of the theoretical model, using the wick

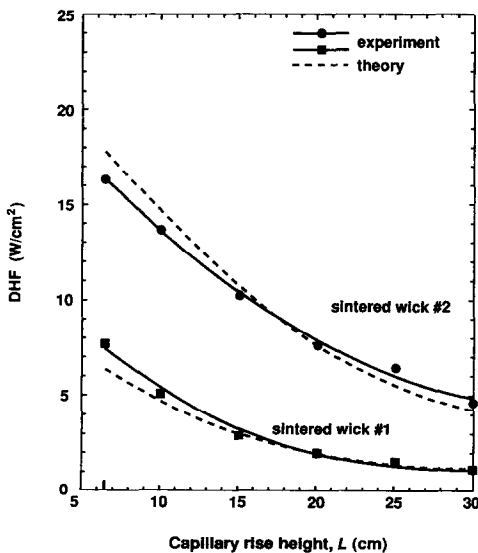


FIG. 7. Experimental and theoretical DHF results vs capillary rise height,  $L$ , for wicks #1 and #2. Solid lines are best fits to the experimental data.

parameters in Table 1, are shown with dashed lines. The theoretical results, in terms of magnitude and trends, are in close agreement with the experimental data, the average difference between the two being less than 10%.

Note that the DHF values in Fig. 7 for wick #2 are substantially above those for wick #1. We should point out that wick #2 was fabricated after tests on wick #1 had been completed. The theoretical model was used in a brief parameter search to obtain estimates of wick dimensions and physical properties that would yield at least a twofold increase in DHF. Therefore, for wick #2, larger and more uniformly sized particles were used (this is apparent in Fig. 5). Fortunately, after sintering and manufacture, wick #2 did indeed possess very desirable properties (i.e.  $r_c$ ,  $k$ ,  $\epsilon$ ). DHF values for wick #2 in Fig. 7 are an average of 3.4 times greater than those for wick #1, with the range being from 2.1 at low  $L$  to 4.3 at large  $L$  [13]. The next section presents the results of a more exhaustive parameter search.

**PARAMETER STUDY**

The influence of wick design parameters on heat pipe performance was studied with the analytical model. Design parameters investigated include wick thickness,  $\delta$ , effective capillary radius of curvature,  $r_c$ , porosity,  $\epsilon$ , and heated diameter,  $D$ . Dryout heat flux values computed as a function of these variables are presented in Figs. 8–14 for cylindrical and flat plate heat pipes of the type depicted in Fig. 2. Water at 1 atm pressure was the coolant and the heater length was  $L_h = 6.4$  cm. These conditions correspond to the laboratory experiments. Unless otherwise noted the default wick structure parameters used for Figs. 8–14 are the values listed in Table 3.

*Parameter effects*

The variation of DHF with wick thickness,  $\delta$ , for a cylindrical wick is shown in Fig. 8; capillary rise

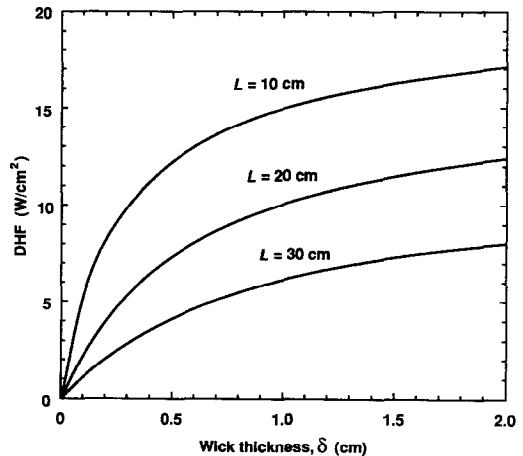


FIG. 8. Theoretical DHF vs wick thickness,  $\delta$ , for  $L = 10, 20$  and  $30$  cm and  $D = 1.28$  cm.

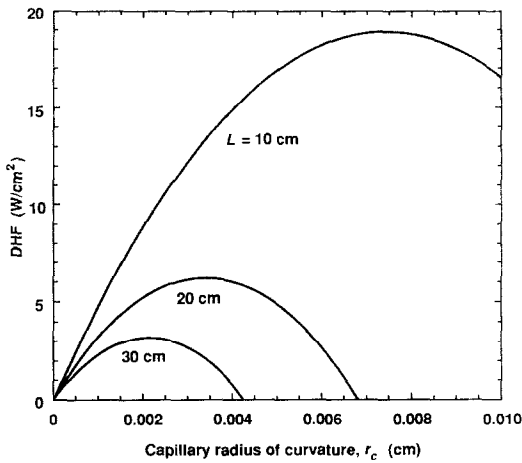


FIG. 9. Theoretical DHF vs effective capillary radius of curvature,  $r_c$ , for  $L = 10, 20$  and  $30$  cm and  $D = 1.28$  cm.

height,  $L$ , is the curve parameter. For the given cylindrical dimensions, DHF increases monotonically with increasing wick thickness. The greatest improvements occur at small wick thicknesses with marginal improvements for  $\delta$  greater than about  $2.0$  cm. The observed monotonic increase in DHF with  $\delta$  is a function of flow path geometries for both the liquid and vapor. A thicker wick structure permits a lower liquid velocity in the wick for a given applied heat flux. The associated lower viscous pressure drop can lead to a higher peak heat flux. In the heated section, a thicker wick tends to decrease the peak heat flux by increasing the vapor pressure drop along the lengthened flow path. With cylindrical geometries this latter effect is attenuated by the radial decrease in superficial vapor velocity as the flow area increases with increasing radius.

Dryout heat flux is plotted against  $r_c$  for a cylindrical wick using  $L$  as the parameter in Fig. 9.

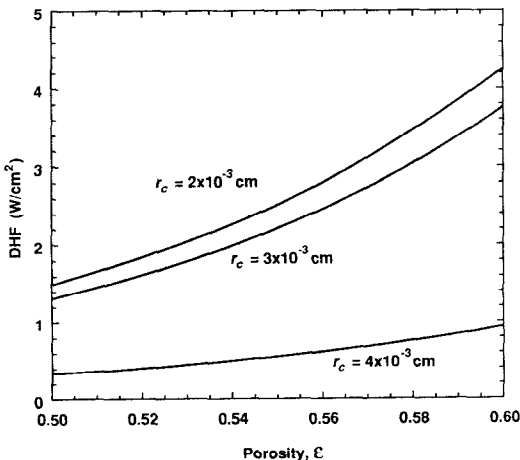


FIG. 10. Theoretical DHF vs porosity,  $\epsilon$ , for three effective capillary radii of curvature,  $D = 1.28$  cm,  $L = 30$  cm.

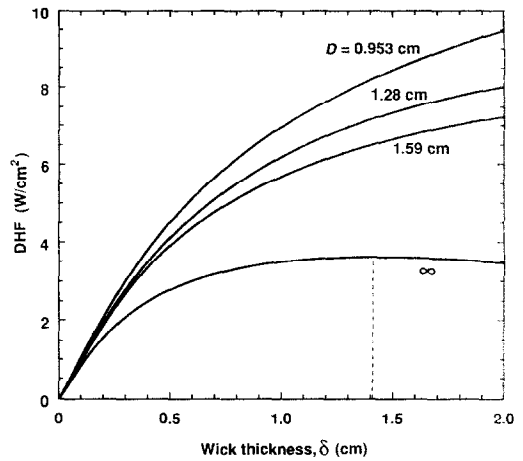


FIG. 11. Theoretical DHF vs wick thickness,  $\delta$ , for three cylindrical wicks and a flat plate wick ( $D = \infty$ ), all at  $L = 30$  cm. The optimum thickness for the flat plate wick is roughly  $1.41$  cm.

An optimum effective capillary radius of curvature appears for each of the three capillary rise heights shown. Optimum values occur due to the influence of  $r_c$  on both bulk permeability and capillary pressure. A large effective radius of curvature results in an increased bulk permeability through equation (1) (for a given porosity,  $\epsilon$ ). This increased permeability decreases flow resistance in the wick, thus increasing peak heat flux capabilities. Conversely a large effective radius of curvature generates low capillary pressure (for a given coolant) through equation (2b). A lower capillary pressure decreases the wick's ability to pump liquid up to the heated section, thus decreasing peak heat flux. The internal balance between these two effects leads to the observed maxima in DHF. Clearly, in a design choice, the effective capillary radius of curvature must be selected to allow for both the capil-

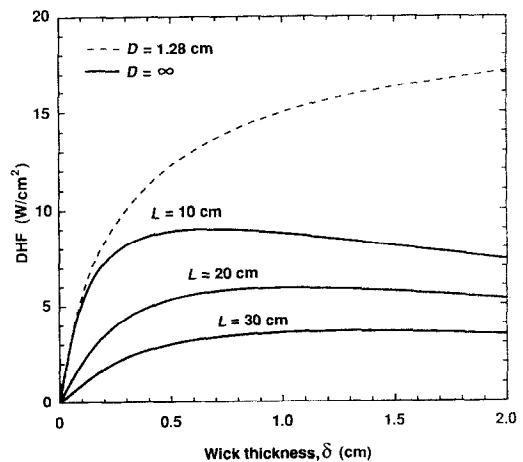


FIG. 12. Theoretical DHF vs wick thickness,  $\delta$ , for a flat plate wick at  $L = 10, 20$  and  $30$  cm. Dashed line is for a cylindrical wick at  $L = 10$  cm from Fig. 8.

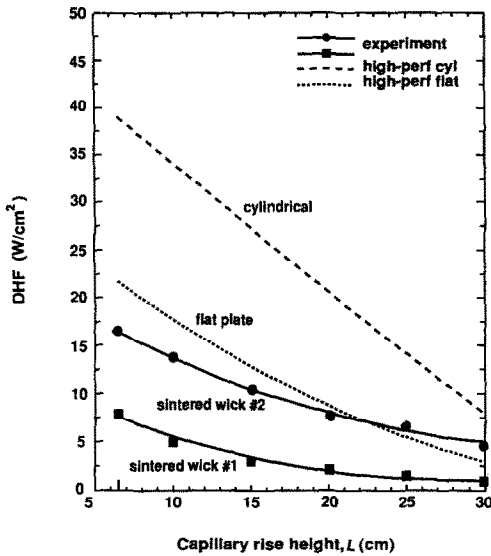


FIG. 13. DHF vs capillary rise height,  $L$ , for the high-performance wick structures and experimental wicks #1 and #2 with  $\theta = 90^\circ$ . Experimental results are from Fig. 7.

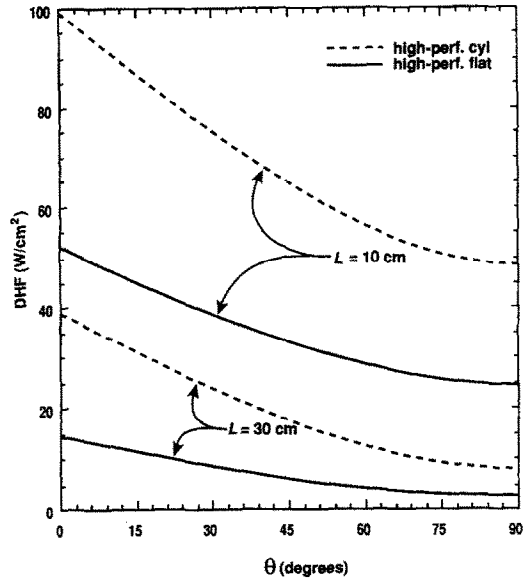


FIG. 14. Theoretical DHF vs tilt angle,  $\theta$ , for the high-performance wick structures with wick lengths of 10 and 30 cm using effective capillary radii of curvature of  $8.35 \times 10^{-3}$  and  $3.58 \times 10^{-3}$  cm, respectively.

lary rise height and heat dissipation needed in an application.

Dryout heat flux is plotted against porosity,  $\varepsilon$ , for three effective capillary radii of curvature in Fig. 10. A cylindrical wick with  $L = 30$  cm is assumed. The three  $r_c$  values vary between the optimal and maximal values for  $L = 30$  cm in Fig. 9. The peak heat flux increases rapidly with increasing porosity for  $r_c = 2 \times 10^{-3}$  and  $3 \times 10^{-3}$  cm. A more gradual increase is seen for  $r_c = 4 \times 10^{-3}$  cm. Small increases in porosity can lead to large improvements in bulk permeability through equation (1), when other parameters are held fixed. As mentioned previously, an increased permeability leads to a lower flow resistance in the wick and thus to higher peak heat fluxes. Porosity of a sintered wick is a function of the sintering process and the particle size distribution. A narrow particle size distribution can lead to increased wick porosity [15].

The effect of heated diameter,  $D$ , on performance is shown in Fig. 11 with DHF plotted against wick thickness,  $\delta$ , for three cylindrical wicks and a flat plate wick, all at  $L = 30$  cm. Dryout heat flux values are seen to decrease with increasing heated diameter at a

given  $\delta$ . In the range of moderate wick thickness,  $\delta < 0.75$  cm, heat pipe performance appears to be a weak function of heated diameter for the three cylindrical wicks. The influence of flat plate vs cylindrical geometry on heat pipe performance with respect to wick thickness is also shown in Fig. 11. As shown previously in Fig. 8, cylindrical wick structures exhibit a monotonic increase in DHF with increasing  $\delta$  over the range shown. For the flat plate wick a peak DHF is observed at roughly  $\delta = 1.41$  cm, beyond which the peak heat flux decreases. The difference in behavior of DHF with wick thickness for the two geometries can be explained in terms of liquid and vapor flow paths. For both cylindrical and flat plate geometries the resistance to liquid flow decreases as the wick thickness is increased. In flat plate wicks the increased resistance to vapor flow through the thicker porous layer is not offset by an increasing flow area as it is in cylindrical geometries. The balance between the decreased liquid resistance and the increased vapor resistance leads to an optimum wick thickness occurring for the flat plate wick. The resulting optimum value for  $\delta$  is a function of the capillary rise height,  $L$ ,

Table 3. Wick structure parameters for parameter study

	Wick thickness, $\delta$ (cm)	Heated diameter, $D$ (cm)	Permeability, $k$ ( $\text{cm}^2$ )	Effective capillary radius, $r_c$ (cm)	Porosity, $\varepsilon$ (%)
Default	0.318	1.28/infinity	$1.430 \times 10^{-7}$	$2.58 \times 10^{-3}$	57
High-performance cylindrical wick	2.000	1.28	$4.250 \times 10^{-7}$	$3.58 \times 10^{-3}$	61
High-performance flat plate wick	0.500	infinity	$4.250 \times 10^{-7}$	$3.58 \times 10^{-3}$	61

as shown in Fig. 12. The dashed curve is from Fig. 8 for a cylindrical wick with  $L = 10$  cm.

The influence of effective capillary radius of curvature,  $r_c$ , and porosity,  $\epsilon$ , on DHF appears to be nearly independent of geometry. Trends for flat plate wicks are not reported here but are similar to those shown in Figs. 9 and 10 for cylindrical geometries.

#### High-performance designs

The foregoing results were used to design high-performance flat plate and cylindrical wick structures. The flat plate wick thickness was chosen to be 0.5 cm to allow a range of operation of  $0 \leq L \leq 30$  cm. A wick thickness of 2.0 cm was chosen for the cylindrical wick as beyond this point only marginal improvements in DHF were predicted. Heater lengths of 6.4 cm were selected, and a heated diameter of 1.28 cm for the cylindrical wick, as these values are identical to those used in the experiments. An effective capillary radius of curvature of  $3.58 \times 10^{-3}$  cm was chosen for both wicks to allow operation to a capillary rise height of 35 cm. It was assumed that porosity could be increased to 60% for both wicks, a slight improvement over that of experimental wick #2. The selected design parameters for the two high-performance wick structures are listed in Table 3. It should be noted that the high-performance design parameters were chosen based upon information presented in Figs. 8–12. These designs do not, however, represent the results of a full optimization study.

Predicted DHF values for the two high-performance structures are plotted against capillary rise height,  $L$ , in Fig. 13. Also shown are the experimental data from Fig. 7 for wicks #1 and #2. The optimized cylindrical wick is theoretically capable of peak heat transfer rates roughly 2.3 times those experimentally measured for sintered wick #2. Further, the rates are almost twice those for the high-performance flat plate wick.

Dryout heat flux predictions are plotted as a function of tilt angle,  $\theta$ , in Fig. 14 for the two optimized structures. A rise height,  $L$ , of 30 cm is assumed for the lower curves. Clearly, the predicted DHF values increase strongly as the tilt angle  $\theta$  is decreased. Thus the experimental and theoretical results shown in Fig. 13 for  $\theta = 90^\circ$  can be expected to increase dramatically as the tilt angle is reduced.

The influence of maximum capillary rise height is also shown in Fig. 14. Results are shown for wick structures with maximum rise heights of  $L = 10$  cm. The 10 cm wicks are identical to the 30 cm high-performance wick structures detailed in Table 3 but with the effective capillary radius of curvature increased to  $8.35 \times 10^{-3}$  cm. The maximum static hold-up height,  $L_{mh}$ , is then reduced to 15 cm. The 10 cm flat plate and cylindrical structures are theoretically capable of DHF values roughly 3.3 and 2.5 times those of the 30 cm wicks. Peak heat fluxes of the order of 50 and 100 W cm<sup>-2</sup>, respectively, are

predicted for the 10 cm flat plate and cylindrical wicks using water as the coolant.

## CONCLUSIONS

A one-dimensional, two-phase model for predicting dryout heat fluxes in sintered-wick heat pipes has been constructed. Predicted dryout heat flux values agree with experimental results for two sintered-copper wicks to within 10%. The influence of wick thickness,  $\delta$ , effective capillary radius of curvature,  $r_c$ , porosity,  $\epsilon$ , and heated diameter,  $D$ , on heat pipe performance was studied parametrically. The parameter study was used to design high-performance flat plate and cylindrical wick structures. High-performance flat plate and cylindrical wicks, 10 cm in length, are shown to be theoretically capable of dissipating 50 and 100 W cm<sup>-2</sup>, respectively, using water as the coolant.

*Acknowledgements*—The authors would like to thank the following individuals: Mr Algerd Basilius of Hughes Aircraft and Dr Roop Mahajan of AT&T for technical counsel; Kim Ann Shollenberger for generating the numerical results; Mr N. Gernert of Thermacore, Inc., for invaluable advice and assistance on wick fabrication; and Mr J. Hunt for the photographs in Fig. 5. Support for this work came from the Semiconductor Research Corporation under Projects Nos. 86-01-070-02 and 87-MP-070-02 and the National Science Foundation through grant No. CBT-8451075.

## REFERENCES

1. A. Faghri, D. B. Reynolds and P. Faghri, Heat pipes for hands, *Mech. Engng* **111**(6), 70–74 (1989).
2. V. I. Tolubinskiy and Y. E. N. Shevchuk, High-temperature heat pipes (survey), *Heat Transfer—Sov. Res.* **20**(1), 79–87 (1988).
3. P. D. Dunn and D. A. Reay, *Heat Pipes*, 3rd Edn. Pergamon Press, Oxford (1982).
4. L. Waller, An old idea may solve VHSIC cooling problem, *Electronics* 19–20 (5 August 1985).
5. A. E. Bergles, High flux boiling applied to microelectronics thermal control, *Int. Commun. Heat Mass Transfer* **15**, 509–531 (1988).
6. A. J. Blodgett, Jr., Microelectronics packaging, *Scient. Am.* **249**, 86–96 (1983).
7. S. Oktay, R. Hannemann and A. Bar-Cohen, High heat from a small package, *Mech. Engng* **108**, 36–42 (1986).
8. A. Basilius, H. Tanzer and S. McCabe, Thermal management of high power PWBs through the use of heat pipe substrates, *Proc. Sixth Annual Int. Electron. Packaging Conf.*, San Diego, California (1986).
9. K. R. Chun, Some experiments on screen wick dry-out limits, *J. Heat Transfer* **94**, 46–51 (1972).
10. F. Ruel, Heat transfer limitations of porous sintered wicks with arteries, *ASME Proc. 1988 Natn. Heat Transfer Conf.*, HTD-96 Vol. 1, pp. 507–515. ASME, New York (1988).
11. B. S. Singh and R. M. Shaubach, Boiling and two-phase flow in the capillary porous structure of a heat pipe. In *Multiphase Transport in Porous Media* (Edited by R. Eaton, K. S. Udell and M. Kaviany), HTD-Vol. 91, pp. 61–68. ASME, New York (1987).
12. D. A. Pruzan, K. E. Torrance and C. T. Avedisian, Two-phase flow and dryout in a screen wick saturated with a fluid mixture, *Int. J. Heat Mass Transfer* **33**, 673–681 (1990).

13. L. K. Klingensmith, Dryout heat-flux performance of sintered copper wicks, Report E-88-08, Sibley School of Mechanical and Aerospace Engineering, Cornell University, Ithaca, New York (1988).
14. D. A. Pruzan, Experimental and analytical investigations into enhanced peak boiling heat transfer from capillary fed porous media, Ph.D. Thesis, Cornell University, Sibley School of Mechanical and Aerospace Engineering, Ithaca, New York (1989).
15. J. Bear, *Dynamics of Fluids in Porous Media*, pp. 47, 166. American Elsevier, New York (1972).
16. M. R. J. Wyllie, Relative permeability. In *Petroleum Production Handbook* (Edited by T. C. Frick), Vol. 2, Chap. 25. McGraw-Hill, New York (1962).

### CONCEPTION DE CALODUCS PERFORMANTS A MECHE FRITTEE

**Résumé**—On présente un modèle analytique pour prédire les limites thermiques de pointe permanente (assèchement) dans des caloducs utilisant des structures de mèche frittée. L'ébullition est prise en compte et on suppose des écoulements monodimensionnels de liquide et de vapeur. Des mesures expérimentales de flux thermique sont faites pour deux mèches cylindriques de cuivre fritté et elles sont comparées aux prédictions analytiques. Les valeurs théoriques et expérimentales d'assèchement s'accordent à mieux que 10%. En utilisant le modèle analytique, on évalue en fonction des paramètres opératoires les performances de caloducs à mèche aplatie ou cylindrique. On identifie des paramètres pour les mèches à haute performance. Des pics à flux thermiques allant respectivement jusqu'à 50 et 100 W cm<sup>-2</sup> sont prédits pour des mèches de 10 cm de longueur avec l'eau comme fluide.

### KONSTRUKTION HOCHEFFIZIENTER WÄRMEROHRE MIT EINEM SINTERDOCHT

**Zusammenfassung**—Es wird ein analytisches Modell zur Berechnung der "dryout"-Grenze bei stationärer Wärmeübertragung in Wärmerohren mit Sinterdocht-Strukturen vorgestellt. In dem Modell werden viele Vorgänge berücksichtigt, und es wird eindimensionale Flüssigkeits- und Dampfströmung angenommen. Für zwei unterschiedliche zylindrische gesinterte Kupferdochte wird die maximale Wärmestromdichte experimentell bestimmt und mit den Berechnungen verglichen. Dabei ergibt sich eine Übereinstimmung innerhalb 10%. Das analytische Modell wird zur Ermittlung des Einflusses der Konstruktionsparameter auf das Verhalten eines Wärmerohres mit ebenem und zylindrischem Docht verwendet. Hierfür werden die Haupteinflußgrößen ermittelt. Für 10 cm lange hocheffiziente Dochte werden mit Wasser als Kühlmittel Spitzenwerte der Wärmestromdichte von 50 bzw. 100 W cm<sup>-2</sup> berechnet.

### РАСЧЕТ ЭФФЕКТИВНЫХ ТЕПЛОВЫХ ТРУБ СО СПЕЧЕННЫМ ФИТИЛЕМ

**Аннотация**—Описывается аналитическая модель для расчета пределов максимального (критического) стационарного теплопереноса в тепловых трубах с использованием структур со спеченным фитилем. Учитывается кипение и предполагается, что течения жидкости и пара являются одномерными. Проводятся экспериментальные измерения максимальных значений теплового потока для двух цилиндрических спеченномедных фитилей, и полученные данные сопоставляются с аналитическими результатами. Теоретические и экспериментальные значения критического теплового потока совпадают с точностью до 10%. На основе аналитической модели оцениваются рабочие характеристики тепловых труб с плоским и цилиндрическим фитилями в зависимости от конструктивных параметров. Определяются параметры эффективных плоского и цилиндрического фитилей. Для эффективных фитилей длиной 10 см, использующих в качестве хладагента воду, рассчитаны максимальные тепловые потоки, составляющие соответственно до 50 и 100 Вт см<sup>-2</sup>.